Chapter

Electrodeposition of Gold Alloys and the Mechanical Properties

Haochun Tang, Tso-Fu Mark Chang, Chun-Yi Chen, Takashi Nagoshi, Daisuke Yamane, Toshifumi Konishi and Katsuyuki Machida

Abstract

Strengthening of electrodeposited gold-based materials is achieved by alloying with copper according to the solid solution strengthening mechanism. Composition of the Au–Cu alloys is affected by the applied current density. The mechanical properties are evaluated by micro-compression tests to evaluate the mechanical properties in microscale to take consideration of the sample size effect for applications as microcomponents in MEMS devices. The yield strength reaches 1.15 GPa for the micropillar fabricated from constant current electrodeposited Au–Cu film, and the film is composed of 30.3 at% Cu with an average grain size of 5.3 nm. The yield strength further increases to 1.50 GPa when pulse current electrodeposition method is applied, and the Cu concentration is 36.9 at% with the average grain size at 4.4 nm.

Keywords: electrodeposition, gold-based alloys, mechanical property, microcompression test, Hall-Petch relationship, solid solution strengthening

1. Introduction

1.1 Application of Au materials in MEMS devices

In recent years, microelectromechanical system (MEMS) capacitive accelerometers have been developed and used in a variety of consumer electronics for acceleration detection in a range of 1–5 G (1 G = 9.8 m/s^2) [1–3]. For applications in medical and health care fields, accurate sensing with sub-1 G detection is necessary to monitor hardly detectable body motions [4, 5]. To detect such low acceleration in a compact sensor module, various types of MEMS accelerometers based on silicon (Si) bulk micromachining have been reported [6, 7]. In order to suppress the thermal-mechanical noise (i.e., Brownian noise (BN) [8]) for the highly sensitive detection, a large proof mass is required. Limited choices of materials for the proof mass and other movable components in a CMOS-MEMS accelerometer have been a major challenge to reduce the BN, which becomes more critical when the parasitic capacitance is reduced in miniaturized devices. Yamane et al. [9–11] propose a miniaturized MEMS accelerometer by using a post-CMOS process with electrodeposited Au in the main components, which enables further size reduction of the proof mass and the device footprint without compromising the sensitivity. With the application of electrodeposited Au in MEMS accelerometers [9–11], a wide range

of acceleration from 1 mG to 20 G can be achieved and are expected to be used in monitoring of hardly detectable body motions.

However, mechanical strengths of Au are much lower than the values of other commonly used materials in electronic devices. For instance, the yield strength of Au is 50–200 MPa in its bulk state [12], and the fracture strength of Si is 1–3 GPa [13], which is one order larger than the strength of Au. The low mechanical strength of Au raises concerns on the structure stability when employed as movable microcomponents. In a study on long-term vibration test of microcantilever made of electrodeposited Au, an obvious tip defection is reported after 10^7 cycles of the vibration [14]. Therefore, strengthening of the Au-based material is necessary to ensure high structure stability for applications in MEMS devices.

1.2 Strengthening mechanisms in electrodeposits

There are four strengthening mechanisms in metallic materials, including work (strain) hardening, grain boundary strengthening, precipitation strengthening, and solid solution strengthening. Except for the work hardening, the other strengthening methods are plausible in the electrodeposits by controlling the electrodeposition conditions. For example, Rashidi et al. [15, 16] report that a finer crystalline grain structure is obtained in the electrodeposited Ni by controlling the electrodeposition parameters such as current density, bath temperature, and additive amount in the aqueous electrolyte. Grain boundary strengthening of the electrodeposited gold is therefore applicable by the grain refinement effect. Classically, the mechanical strength is proportional to inverse square root of the average grain size according to the Hall-Petch Equation [17] given by.

$$\sigma = \sigma_0 + k \cdot d_g^{-0.5} \tag{1}$$

where σ_0 is the friction stress in the absence of grain boundaries, k is a constant, and d_g is the average grain size. In other words, the yield stress increases as the average grain size decreases because pileups in fine-grained materials contain fewer dislocations, and the stress at the tip of the pileup decreases. Thus, a larger applied stress is required to generate dislocations in the adjacent grain. When the average grain size becomes too small, this mechanism breaks down because the grains could not support the dislocation pileups. Typically, breakdown of the Hall-Petch relationship would occur when the average grain size reaches 10 nm in most metals.

Alloying is also one of the commonly applied methods to increase the mechanical strength in electrodeposits. Solid solution strengthening results from the interaction between dislocation and solute atoms can take place. The solute atoms affect the elastic energy of a dislocation due to both local size and modulus changes and act as obstacles to dislocation motions. The alloys could be electrodeposited from a mixed electrolyte containing different metal salts. Schuh et al. [18] reported that the hardness of Ni increased from 1 to 8 GPa by forming Ni–W alloys. Similar strengthening was also reported in Ni–Co [19, 20], Ni–P [21], and Ni–Mn [22] alloys. In addition, alloying of elements having a large difference in the atomic masses would exhibit pronounced strengthening as demonstrated in Cu-based alloys [23].

1.3 Electrodeposition of metallic materials

In metal electrodeposition, current density is often used to control the characteristics in electrodeposits, in particular, grain size. Metal electrodeposition generally follows Butler-Volmer Equation [24], which indicates the current density applied to the electrode is interrelated to the overpotential η:

$$j = j\{\exp(\alpha_a zF\eta/RT) - \exp(\alpha_c zF\eta/RT)\} \quad (2)$$

$$\eta = E - E_{eq} \quad (3)$$

where j is the current density, j_0 is the exchange current density, z is the number of electrons involved in the electrochemical reaction, F is the Faraday constant, R is the universal gas constant, T is the absolute temperature, α_a and α_c are the anodic and cathodic transfer coefficient, η is the overpotential, E is the electrode potential, and E_{eq} is the equilibrium potential. On the other hand, the nucleation rate (ν) of the metal deposited on the electrode is expressed by the following Equation [25]:

$$\nu = a \cdot \exp\left(-b\varepsilon^2/qk_b T|\eta|\right) \quad (4)$$

where a is a proportionality constant, b is the geometrical factor, ε is the surface energy, and q is the required charges for formation of a monolayer. Combining Eqs. (2) and (4), the nucleation rate can be promoted by an increase in the current density, leading to electrodeposits having a finer-grained structure. In addition, electrodeposition can produce not only pure metals but also alloys with controlled compositions. Alloy electrodeposition can realize further enhancement of the mechanical strength based on the solid solution strengthening mechanism [26, 27].

Pulse electrodeposition is a versatile method that has been proven to produce nanocrystalline materials [28, 29]. Pulse electrodeposition parameters (current on-time, current off-time, and pulse current density) play important roles in controlling the electrodeposition process and hence the microstructure and properties of the electrodeposits [30, 31].

1.4 Mechanical properties of small-scale materials

Microcomponents used in MEMS such as microsprings, cantilevers, and structural support could suffer mechanical straining during employment, and mechanical property evaluation of the specimen in microscale is needed. Conventional indentation or wear tests are widely used to characterize mechanical properties of the electrodeposited metallic materials [32]. However, the obtained results are often affected by the substrate, which may not represent the real information of the microcomponents. Moreover, mechanical properties of materials in microscale are much different from those of bulk materials due to the sample size effect [33]. Since Uchic et al. [34] firstly introduced the uniaxial compression testing of micropillars, a new wave of studies of small-scale plasticity has been explored in numerous materials [35–41]. Therefore, micromechanical tests using specimens (i.e., micropillars [40], microcantilevers [42]) in microscale are recognized as the most reliable method to provide reliable information on the mechanical properties for design of MEMS microcomponents.

2. Electrodeposition of Au–Cu alloys from noncyanide electrolyte

Electrodeposition of Au-based alloys is reported for the uses of decorative jewelry, conductive materials in electronic devices, magnetic materials, or catalysts. For applications in MEMS accelerometers, it is particularly important to have properties such as high mechanical strength, high electrical conductivity, and high density. Au–Ni [43, 44] and Au–Co [45] alloys are reported to show improved

mechanical strength, but their magnetic properties may cause the undesired effects in the MEMS devices. Au–Sn alloys are reported to be soft materials and mainly used for soldering [46]. Among these solute elements, Cu has high electrical conductivity and is widely used in electronic devices. Besides the difference of atomic masses between Au and Cu is large, a pronounced effect of solid solution strengthening is expected. The Au–Cu alloys are usually electrodeposited from the alkaline cyanide electrolyte due to the electrolyte stability [47, 48]. However, such strong alkaline electrolyte cannot be used in the lithography process for fabrication of MEMS components, which would cause damage of the photoresists. In this chapter, we utilize the noncyanide electrolyte to electrodeposit Au–Cu alloys and characterize their properties.

2.1 Fabrication of Au–Cu alloys by constant current electrodeposition

The Au–Cu electrolyte used in this work is a commercially available electrolyte provided by MATEX Co., Japan, which contained 17.3 g/L of $X_3Au(SO_3)_2$ (X = Na, K), 1.26 g/L of $CuSO_4$, and EDTA as the additive with pH of 7.5. A potentiostat (Solartron SI1287) is served for applying the constant current. The electrodeposition is carried out at 50 °C, and the current density is varied from 2 to 9 mA/cm^2. A piece of Pt plate and Cu plate with the same dimensions of 1 × 2 cm^2 is used as the anode and the cathode, respectively. Two thicknesses of the films are prepared for the characterization. Thin films with a thickness of ~3 μm are used for surface characterization, and thick films with a thickness of ~50 μm are used only for fabrication of the microcompression specimens.

Figure 1 shows surface morphology of the Au–Cu alloy films electrodeposited at various current density. The films deposited at lower current densities exhibited nodular-like structures as shown in **Figure 1(a)** and **(b)**. When a higher current density is used (4–7 mA/cm^2), the surface morphology gradually changes to smooth surface condition as shown in **Figure 1(c)**–**(f)**. Large agglomerates of bump clusters are observed on the surface when the current density is higher than 8 mA/cm^2, as shown in **Figure 1(g)** and **(h)**. Similar morphology is reported for the Au-based alloys electrodeposited at high current density [48].

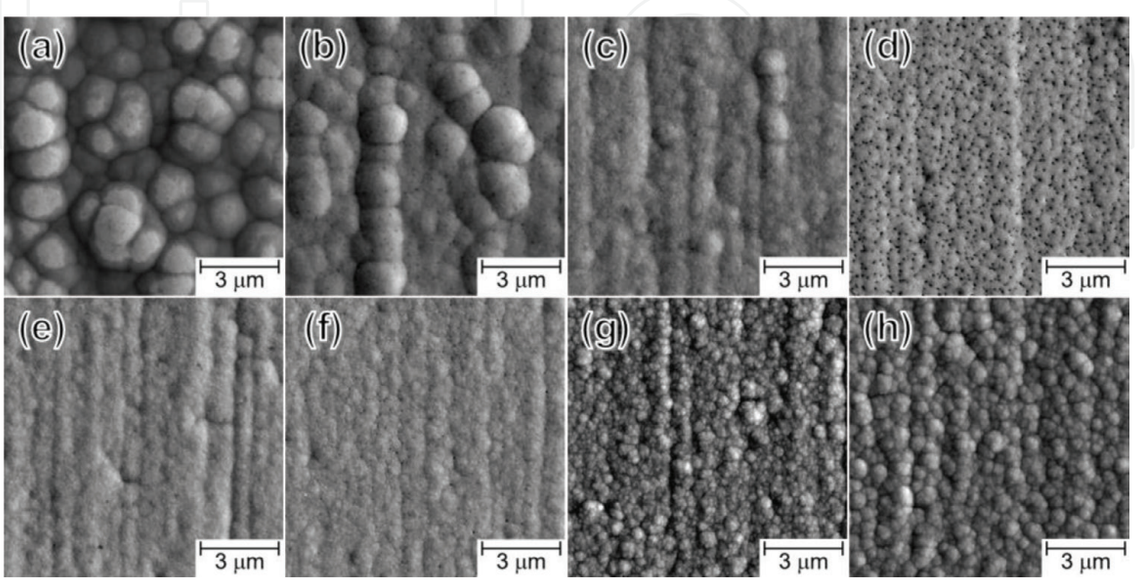

Figure 1.
SEM micrographs of the Au–Cu alloy films electrodeposited at current density (a) 2, (b) 3, (c) 4, (d) 5, (e) 6, (f) 7, (g) 8, and (h) 9 mA/cm^2.

2.2 Crystalline structure and chemical composition of electrodeposited Au–Cu alloys

Figure 2 shows XRD patterns of the Au–Cu alloys electrodeposited at current densities ranging from 2 to 9 mA/cm^2. Both the (111) and (200) peaks shift continuously to a higher diffraction angle as the current density increases. For instance, the (111) peak shifts from 2θ = 38.79° at the current density 3 mA/cm^2 to 2θ = 40.09° at the current density 8 mA/cm^2. The peak shift is suggested to be a result of the increase in the Cu content since the lattice constants of Cu are larger than that of Au. No diffraction peaks from intermetallic nor other ordered phases are observed in the electrodeposited films. Relationships between the current density with average grain size, Cu concentration, and the lattice constant are summarized in **Figure 3**. The average grain sizes are estimated from the XRD results and the Scherrer equation. The grain size is reduced from 8.8 nm to a minimum value of 5.3 nm when the current density is increased from 2 to 6 mA/cm^2. Grain size of electrodeposited materials is highly dependent on the overpotential, in which grain refinement is observed as the overpotential increased [49]. Based on the Butler-Volmer equation, the overpotential is interrelated to the current density, in which the overpotential increases as the current density increases. Therefore, it is expected to see a reduction in the grain size as the current density increases.

On the other hand, an increased in the grain size is observed when the current density increases beyond 6 mA/cm^2. Increasing the current density also promotes side reaction(s), such as hydrogen evolution. Because of this, overpotential of the main reactions, which are reduction of Au and Cu in this study, would be lowered when the side reaction(s) is promoted [50]. This should be the cause of the grain

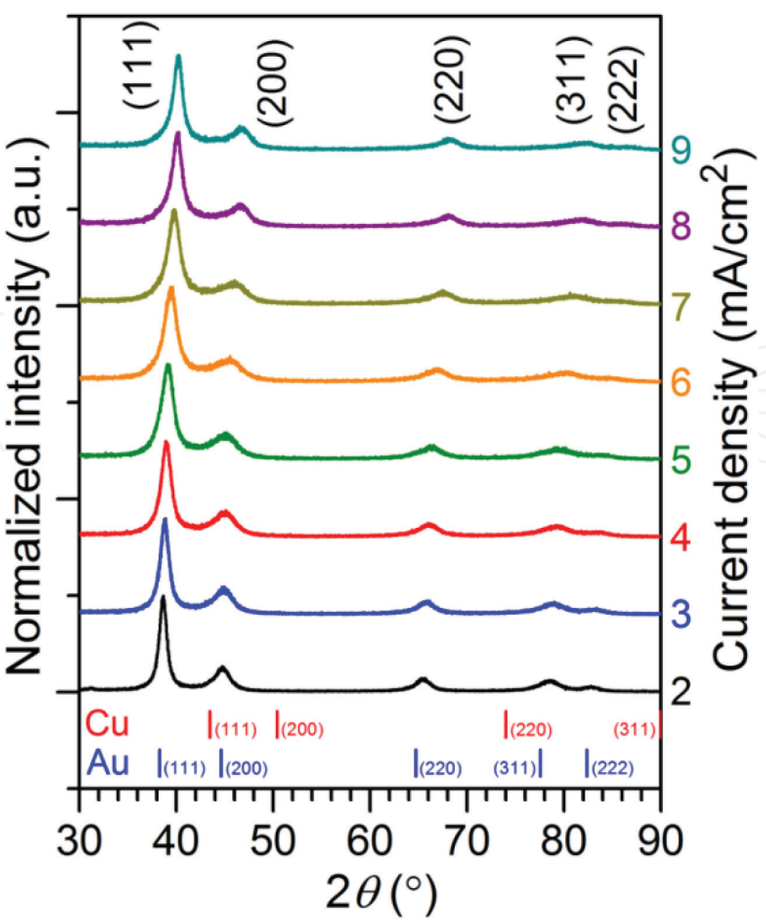

Figure 2.
XRD patterns of the Au–Cu alloy films electrodeposited at varied current density.

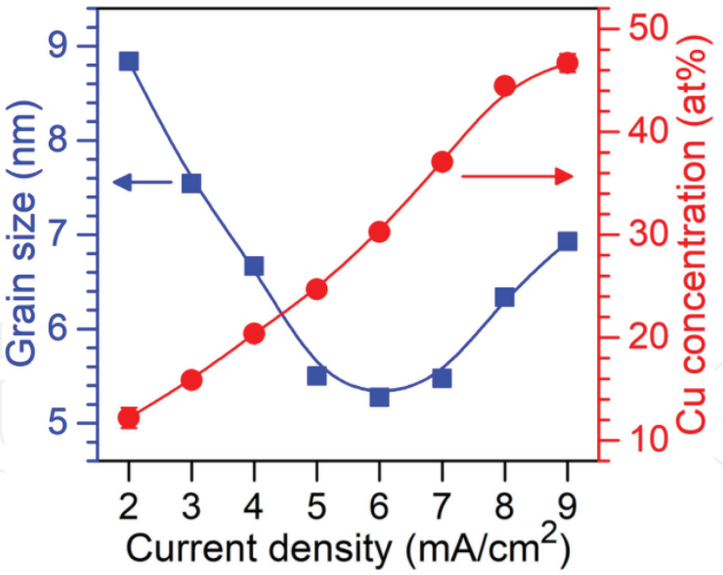

Figure 3.
Plots of the current density versus grain size and Cu concentration.

coarsening observed when the current density is higher than 6 mA/cm^2. Meanwhile, a sustained increase of the Cu concentration from 12.2 to 46.7 at% is observed when the current density is increased from 2 to 9 mA/cm^2. The results can be interpreted by the difference in the standard reduction potential between Au and Cu [51]. The standard reduction potential of Cu is more negative than that of Au. An increase in the cathodic current density would make the applied potential to be more negative; hence, reduction of Cu is gradually favored and leads to an increase in the Cu concentration.

2.3 Fabrication of Au–Cu micropillars and micromechanical properties

Micromechanical properties of the Au–Cu alloys are evaluated using micropillars fabricated from the thick Au–Cu films by focus ion beam (FIB, Hitachi FB2100). Fabrication process of micropillar is shown in **Figure 4**. The Au–Cu micropillars have square cross section of 10 × 10 μm^2 and height of 20 μm. The microcompression tests are conducted with a testing machine specially designed for microspecimens. The compression is conducted at a constant displacement rate of 0.1 μm/s using a piezoelectric actuator.

Figure 5 shows SIM images of the Au–Cu alloy micropillars fabricated from the thick Au–Cu alloy films before and after the microcompression tests. Barrel-shape deformations are observed in the micropillars fabricated from the films electrodeposited at current density 3, 5, and 6 mA/cm^2, which are typical deformation behaviors for polycrystalline metallic materials [52, 53]. When the current density is further increased to 8 mA/cm^2, brittle fractures indicated by the cracks along

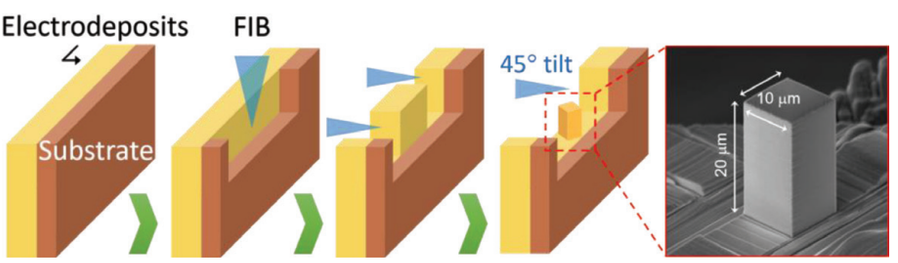

Figure 4.
Fabrication process of micropillars by FIB.

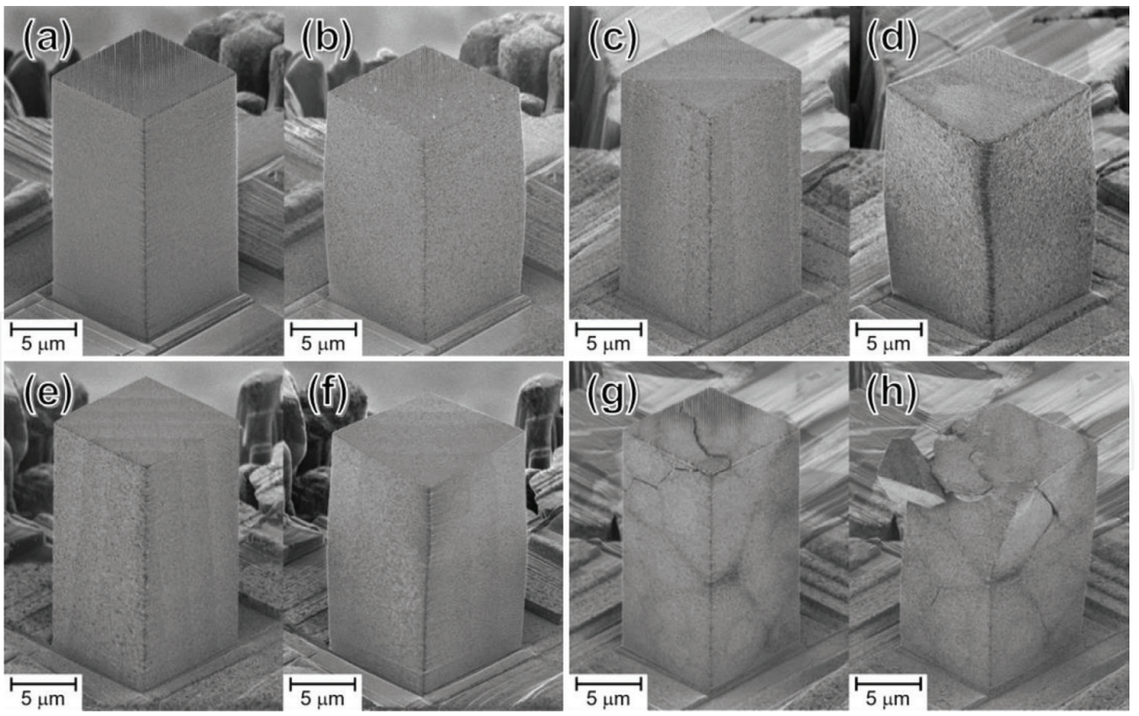

Figure 5.
SIM images of the Au–Cu alloy micropillars fabricated from the films electrodeposited at current density (a,b) 3, (c,d) 5, (e,f) 6, and (g,h) 8 mA/cm². (a,c,e,g) Before and (b,d,f,h) after microcompression tests.

boundaries of the agglomerates are observed after the compression test. The Au–Cu alloy film electrodeposited at 8 mA/cm^2 is composed of nano-grains, which is similar to the film electrodeposited at lower current density of 3 mA/cm^2; however, formation of the bump-clustered agglomerates at high current density might be the main cause of the brittle deformation. Au–Cu alloys are known to be highly ductile materials. To the best of our knowledge, this is the first report on brittle fracture of Au–Cu alloys, and this information is essential for the design of components used in MEMS devices.

Engineering strain-stress (*SS*) curves obtained from the microcompression tests are shown in **Figure 6**. Generally, all the pillars exhibit extremely high yield stress (σ_y, determined by the cross-point of the *SS* curve and 0.2% offset line of the elastic deformation region) ranged at 1.00–1.15 GPa, which are far larger than the yield

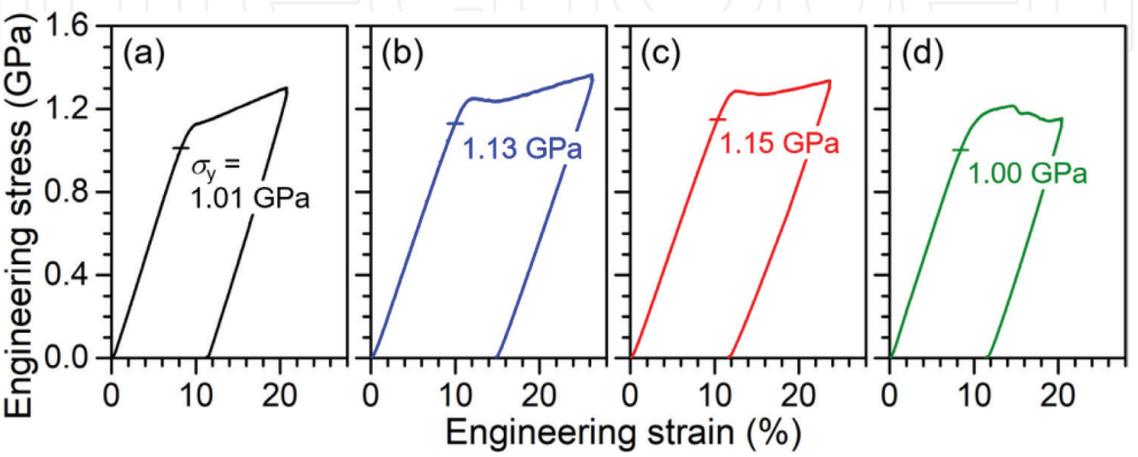

Figure 6.
Engineering strain-stress curves of the micropillars fabricated from the films electrodeposited at current density of (a) 3 mA/cm², (b) 5 mA/cm², (c) 6 mA/cm², and (d) 8 mA/cm². The yield strength (σ_y) in each curve is marked by a horizontal bar.

stress obtained from micromechanical tests of pure Au and pure Cu reported in the literature [52, 54]. Flow stresses (σ_f) at 10% plastic strain of all the micropillars are higher than 1.3 GPa except for the micropillar prepared from the film electrodeposited at current density of 8 mA/cm^2, in which the crack-induced brittle fracture should be the reason of the lowered flow stress.

The enhanced yield stress in the Au–Cu alloys is mainly attributed by the following two mechanisms: (i) grain boundary strengthening [17] and (ii) solid solution strengthening [26, 27]. As shown in **Figure 3**, the grain refinement effect goes along with an increase in the Cu concentration as the current density increases. According to the grain boundary strengthening mechanism, the strength of metallic materials increases as the total amount of grain boundary in a specimen increases, which is also understood as a decrease in the average grain size. Moreover, the solid solution strengthening mechanism could restrict the dislocation movement due to interaction of the dislocations with the strained lattice surrounding the solute atoms, which then leads to a stacked strengthening beyond the grain boundary strengthening mechanism.

3. Pulse current electrodeposition of ultrahigh strength nanocrystalline Au–Cu alloys

3.1 Fabrication of Au–Cu alloys by pulse current electrodeposition

The Au–Cu alloys are electrodeposited on cold-rolled Cu substrates with a commercially available electrolyte (see Section 2.1). Temperature of the electrolyte is maintained at 50 ± 1°C using a water bath. The pulse current electrodeposition is carried out using a pulse power supply (plating electronic GmbH, type pe86CB-20-5-25-S/GD). For all experiments, the current on-time (t_{on}) is fixed at 10 ms, while the pulsed current density (J_p) and the current off-time (t_{off}) are varied. The parameters are summarized in **Table 1**. Thin Au–Cu alloy films with a thickness of 3–5 μm are used for characterization of the composition, grain size, and morphology. Thick films (thickness ~50 μm) are prepared for fabrication of the microcompression specimens.

3.2 Effects of the pulse current density

Figure 7(a) shows XRD patterns of the Au–Cu alloys electrodeposited at the J_p of 5–20 mA/cm^2 with the t_{on} and t_{off} both fixed at 10 ms. All electrodeposits show the same crystal structure, in which all of the peaks could be indexed to the face-centered cubic (fcc) reflection. With an increase in the J_p, the peaks shift to larger diffraction angles due to the lattice shrinkage caused by the increase in the Cu concentration. Effects of the J_p on the Cu concentration and grain size are plotted in **Figure 7(b)**. The copper concentration linearly increases from 15.3 to 41.2 at% as

Operating parameters	Range
Pulse current density (mA/cm^2)	5–60
Current on-time (ms)	10
Current off-time (ms)	5–600
Electrolyte temperature (°C)	50

Table 1.
Parameters for pulse electrodeposition of Au–Cu alloy films.

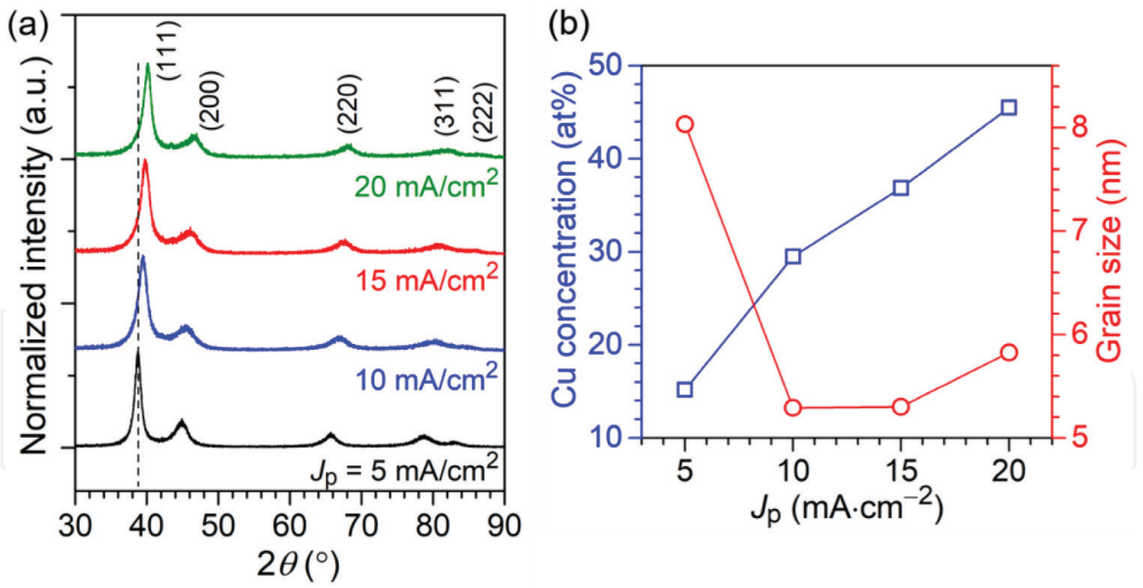

Figure 7.
(a) XRD patterns of the Au–Cu alloys electrodeposited at the J_p varied from 5 to 20 mA/cm² with t_{on} and t_{off} both fixed at 10 ms. The straight dash line indicates the center of (111) diffraction peak in the J_p of 5 mA/cm² sample. (b) Plot of the J_p versus the grain size and Cu concentration.

the J_p increases from 5 to 20 mA/cm^2. These results are similar to the Au–Cu alloys prepared by the constant current electrodeposition, in which an increase in the J_p leads to a higher Cu concentration. The standard reduction potential of Cu^{2+} ions is more negative than that of Au^+ ions [51]. An increase in the J_p makes the applied potential to be more negative; therefore, the reduction of Cu^{2+} is gradually favored and leads to an increase in the Cu concentration. In the meanwhile, the grain size decreases from 8.0 nm to a minimum value of 5.2 nm as the J_p increases from 5 to 10 mA/cm^2, which is attributed to the increase of the nucleation rate as the current density increases [49]. On the other hand, after reaching the minimum value, the grain size increases to 5.8 nm as the J_p increases to 20 mA/cm^2. The grain growth at high J_p could be attributed to the promoted side reactions (i.e., hydrogen evolution) as the applied potential becomes more negative, which then lowers overpotential of the main reaction(s) (reductions of Au^+ and Cu^{2+} in this case). The grain size of electrodeposits is highly dependent on the overpotential, and the grain size increases when the overpotential is lowered [49].

3.3 Effects of current off-time

Effects of the t_{off} on crystal structure and alloy composition of the Au–Cu alloys are discussed in this section. **Figure 8** shows XRD patterns of the Au–Cu alloys electrodeposited at the J_p of 20 mA/cm^2 and the t_{off} varied from 20 to 120 ms. Similar to **Figures 3** and **7(a)**, all the XRD patterns show the fcc reflections, and no other diffraction peak is observed. The major (111) peak gradually shifts from 2θ = 40.2° to 38.8° when the t_{off} increases from 20 to 120 ms, which indicates a decrease in the Cu concentration. It is known that the t_{off} plays an important role in controlling the alloy composition due to the galvanic displacement reaction occurred on the substrate surface [55–58]. During of the off-time period, nobler metals continue to be deposited on the substrate surface, and less noble metals on the substrate surface would be oxidized and dissolved away. The displacement reaction leads to a decrease in concentration of the less noble component in the alloy. In the present Au–Cu system, the standard reaction potential of Au is more positive than Cu; hence, nobleness of Au is higher. Therefore, the displacement reaction occurred during the

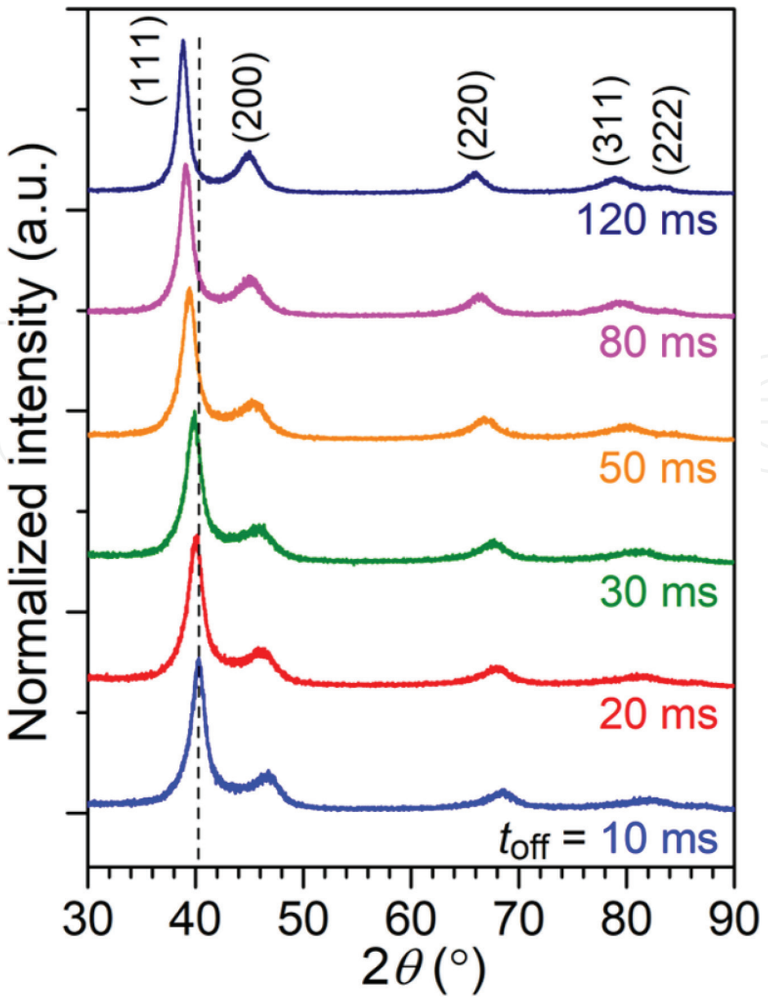

Figure 8.
XRD patterns of the Au–Cu alloys electrodeposited at the J_p of 20 mA/cm² with the t_{off} varied from 10 to 120 ms. The t_{on} was fixed at 10 ms. The straight dash line indicates center of the (111) diffraction peak in the t_{off} of 10 ms sample.

off-time period causes a decrease in copper concentration in the Au–Cu alloy, which is consistent with the lattice swelling observed from the XRD results.

Dependence of the Cu concentration and grain size on the t_{off} as the J_p varies from 10 to 60 mA/cm² is shown in **Figure 9**. Several trends are observed as the J_p and the t_{off} change. Firstly, a decrease in the Cu concentration is observed as the t_{off} increases at all of the J_p. The results correspond well with those observed from the XRD patterns, in which more Cu is replaced by Au as the t_{off} increases. Secondly, when the t_{off} increases, decreasing rate of the Cu concentration shows a transition from high to low as indicated by the change in slope of the curves in **Figure 4(a)**. The J_p of 50 mA/cm² curve indicates this point clearly. Cu concentration of the Au–Cu alloy shows a steep decrease from a short t_{off} to t_{off} of 240 ms, and the slope becomes less steep at t_{off} longer than 240 ms. The slope is suggested to be related to the displacement reaction or dissolution rate of Cu component in the Au–Cu alloy, in which a steep slope indicates a high Cu dissolution rate. Again, the result is expected since the Cu dissolution rate is directly related to concentration of Cu component at the surface of the film, and the Cu concentration is higher at the moment when the electrodeposition just entered the off-time period. Then the Cu concentration gradually decreases and leads to a lower Cu dissolution rate. Thirdly, the decreasing rate of Cu concentration is slowed down as the J_p increases. The evidence can be clearly seen in the J_p of 20 mA/cm² and J_p of 60 mA/cm² cases. The Cu concentration decreases from 36.9 to 18.4 at% when the t_{off} is increased from 30

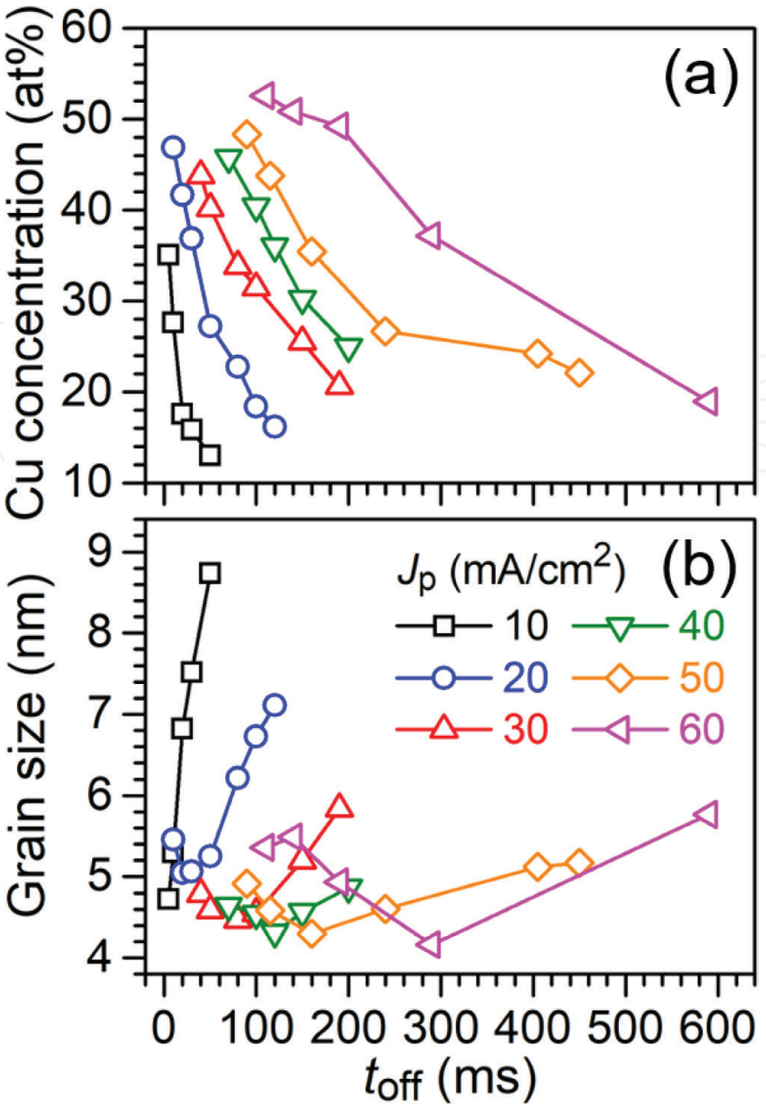

Figure 9.
Plots of the t_{off} versus (a) grain size and (a) Cu concentration at varied J_p.

to 100 ms in the case of the J_p of 20 mA/cm^2. A much longer t_{off} is required, from 290 to 590 ms, for the Cu concentration to decrease from 37.1 to 18.9 at% in the case of the J_p of 60 mA/cm^2. The alloys electrodeposited at higher J_p contain higher Cu concentration. Although the dissolution rate is highly dependent on the Cu concentration, diffusion of Cu^{2+} away from surface of the substrate and Au^{+} from the bulk to the reaction site could also affect the dissolution rate. Hence, a longer t_{off} is needed to reach the same Cu concentration when the J_p is high.

Effects of the t_{off} on the grain size show similar trends at various J_p, in which the grain size initially decreases to a minimum value of ca. 4.40 nm and then the grain size reversely increases when the t_{off} increases. The displacement reaction occurred during the off-time period can initiate rearrangement of atoms in the alloy, which could induce nucleation or grain growth of the reduced metals in the alloy. The driving force of the rearrangement is dependent on the dissolution rate. When the driving force is high, the rearrangement is more vigorous, and nucleation is induced. As shown in **Figure 9(a)** and **(b)**, the grain size reduces with a decrease in the Cu concentration until reaching ca. 35 at%. On the other hand, the rearrangement is less vigorous, and grain growth is favored when the Cu concentration is low. This is why grain coarsening is observed when the Cu concentration is lower than ca. 35 at% as the t_{off} increases.

As a result, a wide Cu concentration ranging from 10.1 to 53.0 at% is attained by adjusting either or both the J_p and the t_{off}. In addition, the critical point observed

at the Cu concentration of ca. 35 at% indicates the grain size is interrelated to the alloy composition. **Figure 10** shows the grain size as a function of the Cu concentration. The Cu concentration and the grain size basically follow a monotonic relationship. Similar behavior is reported in other pulse current electrodeposited alloys [58, 59]. When compared to the constant current electrodeposited Au–Cu (square symbols), the constant current electrodeposited Au–Cu also shows the same monotonic relationship. Furthermore, the pulse current electrodeposition allows fabrication of Au–Cu alloys with a wider range of the Cu concentration and a much finer-grain size than those of the constant current electrodeposition, which are both advantageous for applications as movable microcomponents.

3.4 Morphology of pulse electrodeposited Au–Cu alloys

Effects of the pulse current electrodeposition parameters on morphology of the Au–Cu films are observed by the SEM as shown in **Figure 11**. The overview of the Au–Cu alloys electrodeposited at the J_p of 15 mA/cm^2 shows bright surfaces when the t_{off} is between 20 to 50 ms. From **Figure 11(a)**, the alloy film electrodeposited at the t_{off} of 20 ms shows pebble-like structures, and size of the pebble-like structures shrinks gradually as the t_{off} increases to 50 ms as shown in **Figure 11(b)** and **(c)**. The surface becomes dull when the t_{off} increases to 100 ms, and the pebble-like structures are still observed as shown in **Figure 11(d)**. When a lower J_p at 5 mA/cm^2 is used, two alloy films deposited at the t_{off} of 30 and 100 ms both show dull surface. The size of the pebble-like structures increases as the t_{off} increases to 100 ms (**Figure 11(f)**). The surface condition becomes very rough when the J_p is increased to 20 mA/cm^2. As shown in **Figure 11(g)**, the alloy film deposited at the J_p of 20 mA/cm^2 and the t_{off} of 20 ms shows large agglomerates of colony-like clusters, and dull surface is observed. Then the surface becomes bright, and the size of the pebble-like structures decreases as the t_{off} increases to 50 ms, shown in **Figure 11(h)**. An interesting conclusion could be made here, in which Au–Cu alloys with similar surface morphology and similar Cu

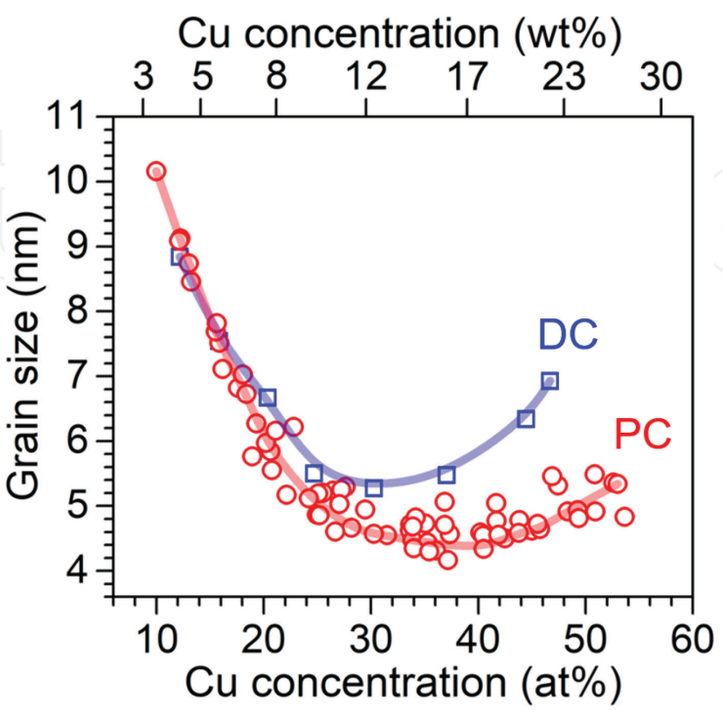

Figure 10.
A plot of relationship between grain size and Cu concentration for Au–Cu alloys electrodeposited with varied J_p and t_{off}.

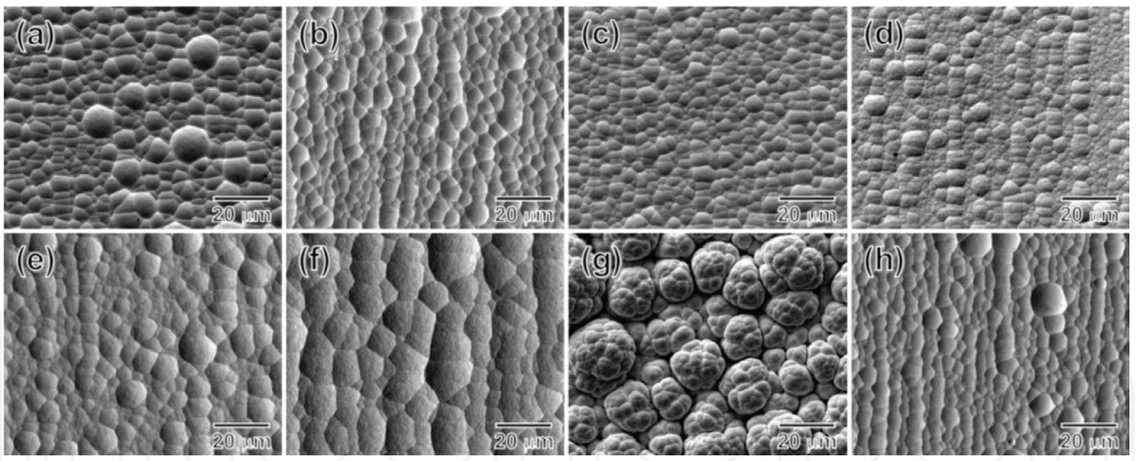

Figure 11.
SEM micrographs of the Au–Cu alloy thick films. The alloys electrodeposited at the J_p of 15 mA/cm² with the t_{off} of (a) 20 ms, (b) 30 ms, (c) 50 ms, and (d) 100 ms; J_p of 5 mA/cm² with (e) 30 ms and (f) 100 ms; J_p of 20 mA/cm² with (g) 20 ms and (h) 50 ms. The t_{on} is fixed at 10 ms.

concentration could be fabricated using different pulse parameters (**Figure 11(b)**: J_p = 15 mA/cm², t_{off} = 30 ms; **Figure 11(h)**: J_p = 20 mA/cm², t_{off} = 50 ms). This result demonstrates that not only the grain size but also the surface morphology is interrelated to the Cu concentration. The morphology, composition, grain size, and electrodeposition parameters of the Au–Cu alloy thick films are summarized in **Table 2**.

Effects of the J_p and the t_{off} on the morphology and the Cu concentration are summarized and illustrated in **Figure 12**. In general, roughness of the surface is affected by the current density, and smoothness of the surface is related to the displacement reaction, i.e., dissolution of the Cu component in the Au–Cu alloy. In other words, an increase in the J_p leads to roughening of the surface, and promotion of the displacement reaction causes smoothening of the surface. For example, when a high J_p and a short t_{off} are applied, a rough surface would be formed during the on-time period because of the high J_p, and the smoothening effect caused by the displacement reaction would be insufficient because of the short t_{off}. In this case, a rough surface condition is obtained as shown in **Figure 11(g)**. When a high J_p and a long t_{off} are applied, although the high J_p would give a rough surface, but with a long enough t_{off}, the displacement reaction could cause enough smoothening effect to produce a smooth surface. On the other hand, when a low J_p is used, the surface

J_p, mA/cm²	t_{off}, ms	[Cu], at%	d_g, nm	Morphology
20	20	46.4	4.8	Colony-like clusters and dull surface
	50	33.9	4.7	Pebble structure and bright surface
15	20	36.9	4.7	Pebble structure and bright surface
	30	34.2	4.8	Pebble structure and bright surface
	50	29.5	4.9	Pebble structure and bright surface
	100	21.2	6.2	Pebble structure and dull surface
5	30	18.0	7.0	Pebble structure and dull surface
	100	12.1	9.1	Pebble structure and dull surface

Table 2.
A summary of pulse parameters, Cu concentration ([Cu]), grain size (d_g), and morphology of the Au–Cu alloys.

would be less rough than the one using high J_p. However, the Cu concentration is low when a low J_p is used, and this limits the displacement reaction, that is, the surface smoothening effect. As observed in the alloys electrodeposited at the J_p = 5 mA/cm^2 in **Figure 11(e)** and **(f)**, the surface condition does not become smoother as the t_{off} increases from 30 to 100 ms.

3.5 Micromechanical properties of pulse electrodeposited Au–Cu alloys

Micromechanical properties of the pulse current electrodeposited Au–Cu alloys are evaluated by microcompression tests to demonstrate the potential for applications in microelectronic devices. The micropillars with the same dimensions of 10 × 10 × 20 μm^3 are fabricated from the thick Au–Cu films by FIB. **Figure 13** shows SIM images of 6 Au–Cu micropillars with different alloy compositions after the microcompression tests. Typical polycrystalline deformation (barrel-shape) is observed in the micropillars at the Cu concentration below ~35 at% (**Figure 13(a)–(d)**). As the Cu concentration increases to ~37 at%, the deformation behaviors change into brittle fracture (**Figure 13(e)**). For the Cu concentration of 46.4 at% pillar (**Figure 13(f)**), the brittle fracture occurs from the crack boundaries originating from the large agglomerates as observed in **Figure 11(g)**. The large agglomerates and the brittle fracture are also observed in the constant current Au–Cu alloys electrodeposited using a high current density, in which the brittle fracture is observed when the Cu concentration is higher than 37 at% (**Figure 5(g)** and **(h)**).

Engineering strain–stress (SS) curves obtained from the microcompression tests are shown in **Figure 14**. The σ_y's are estimated from the 0.2% offset line of the elastic deformation region. Similar to the constant current Au–Cu micropillars, the σ_y increases with an increase of Cu concentration and a decrease of grain size until the Cu concentration reaches ~34 at% (**Figure 14(a)–(d)**). For the Cu concentration of 37

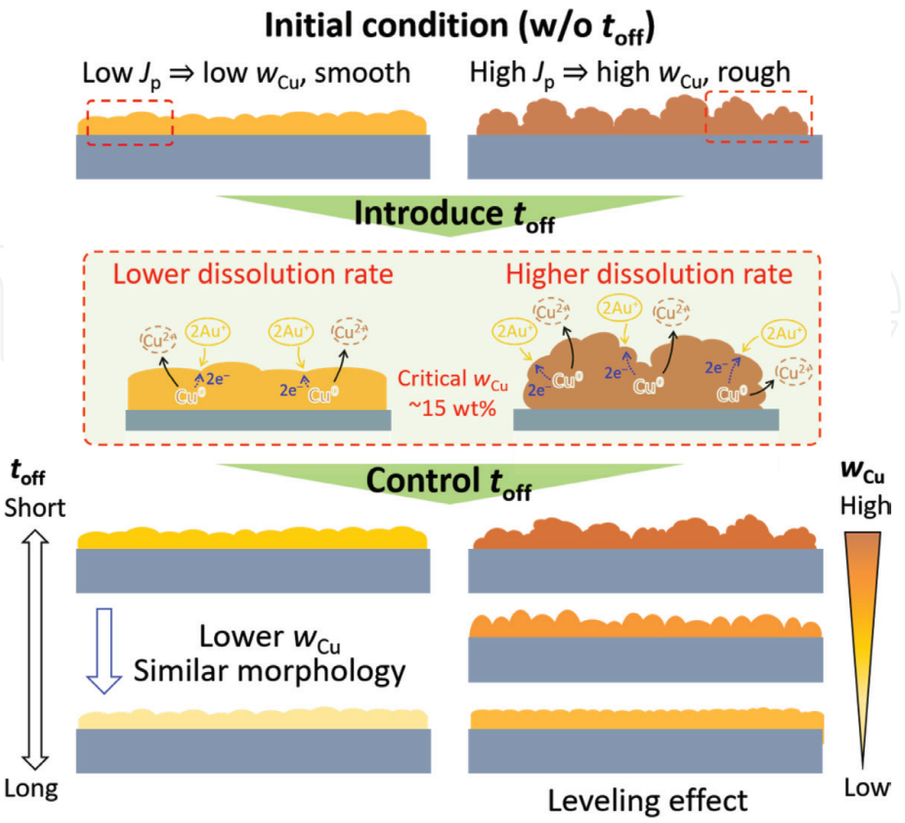

Figure 12.
Illustration of the morphology change with the pulse electrodeposition parameters.

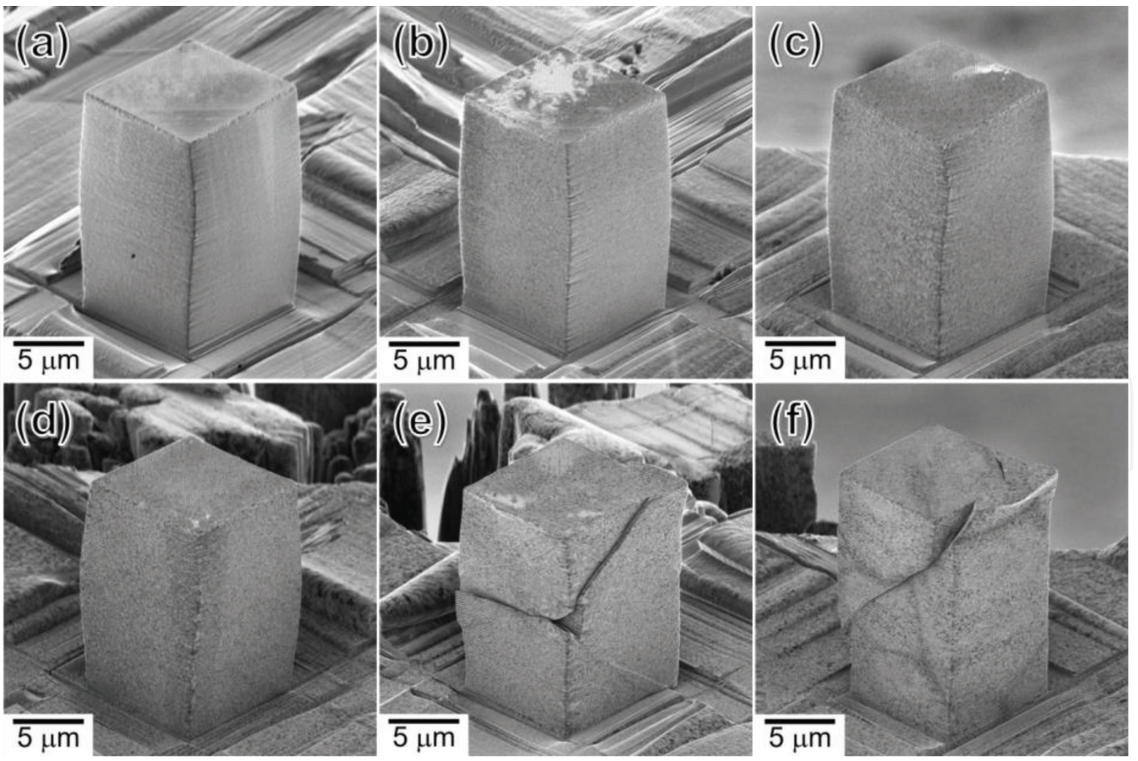

Figure 13.
SIM micrographs of the pulse current Au–Cu micropillars after compression tests. The micropillars were fabricated from the thick Au–Cu with the Cu concentration of (a) 12.1 at%, (b) 15.6 at%, (c) 21.2 at%, (d) 34.2 at%, (e) 36.9 at%, and (f) 46.4 at%.

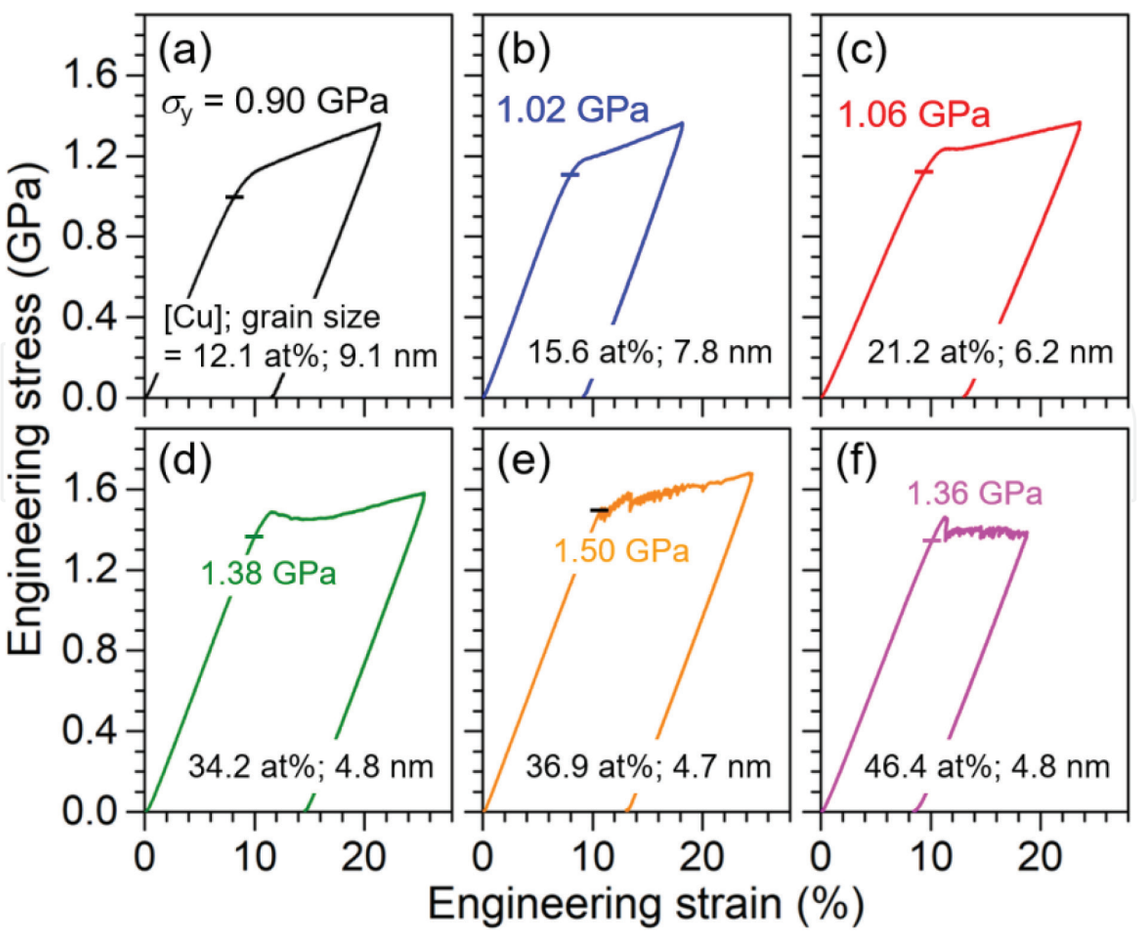

Figure 14.
Engineering SS curves of the micropillars containing the Cu concentration of (a) 12.1 at%, (b) 15.6 at%, (c) 21.2 at%, (d) 34.2 at%, (e) 36.9 at%, and (f) 46.4 at%. The yield strength σ_y is marked by a horizontal bar.

at% micropillar, the σ_y reaches the highest value of 1.50 GPa. However, the subsequent flow stress behaviors are different with the lower Cu concentration micropillars, which are attributed to the difference in the deformation behaviors. The brittle fracture in the Cu concentration of 36.9 at% and 46.4 at% micropillar (**Figure 11(e)** and **(f)**) leads to the stagnant and trembling flow stress after the yielding points.

3.6 Strengthening mechanisms in electrodeposited Au–Cu alloys

The σ_y ranges from 0.90 to 1.50 GPa in the constant current- and pulse current electrodeposited Au–Cu micropillars, which can be understood as synergistic effects of the grain boundary strengthening [17] and the solid solution strengthening mechanisms [26, 27]. According to the grain boundary strengthening mechanism [17], the strength of metallic materials increases as total amount of grain boundary in a specimen increases, which is also understood as a decrease in the average grain size. Moreover, the solid solution strengthening mechanism [26, 27] is considered to restrict the dislocation movement due to interaction of the dislocations with the strained lattice surrounding the solute atoms, which then leads to a stacked strengthening beyond the grain boundary strengthening mechanism. In **Figure 15**, the grain boundary strengthening mechanism can be summarized as the Hall-Petch plots (σ_y vs. (grain size)$^{-0.5}$) using the results presented in this study and the literature [47, 48, 60]. Due to lack of the literature on the yield stress of Au–Cu alloys, the results obtained from Vicker microhardness (HV) tests are adopted and converted to the yield stress by dividing the microhardness value to a Tabor coefficient of 4 (σ_y = HV/4 [61]) for the comparison.

Overall, the values reported in the literature all follow the Hall-Petch relationship. However, softening caused by the inverse Hall-Petch effect occurs when the grain size scales down to ~6 nm. The results presented in this work also follow the Hall-Petch relationship well. Most importantly, the results obtained in this study are much more reliable than those of Vicker microhardness tests since the hardness results are often

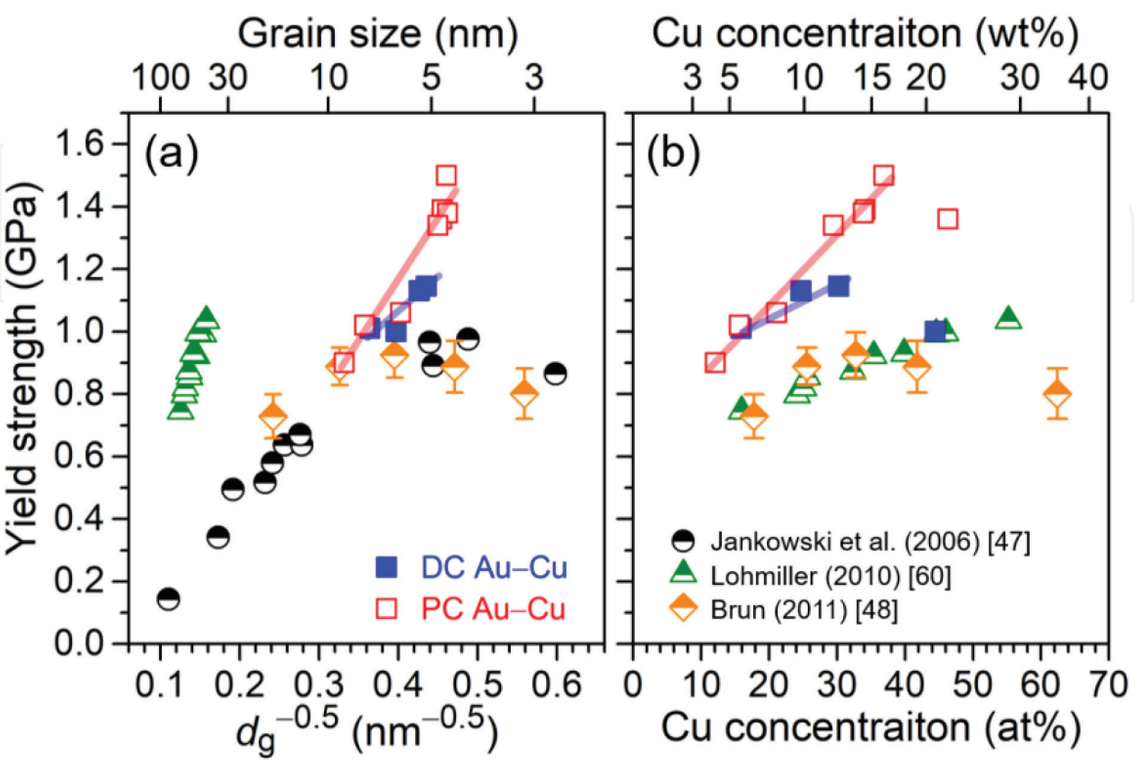

Figure 15.
Plots of (a) inverse square root of the grain size (d_g) and (b) Cu concentration versus the σ_y.

affected by the substrate, which cannot reflect real strength of the electrodeposited films. A number of theories for solid solution strengthening have proposed that the strength is proportional to the solute concentration with order of 1/2 [Fleischer (1963)] or 2/3 [Labusch (1970)], which depends on the solute concentration. It is worth noticing that the highest σ_y at 1.38 GPa obtained in the pulse current electrodeposited Au–Cu micropillar is higher than that of constant current electrodeposited micropillar with the same Cu concentration (σ_y = 1.15 GPa), demonstrating the capability to further refine the grain size and enhance the strength by pulse current electrodeposition.

4. Conclusions

In the present study, high-strength Au–Cu alloys with nanocrystalline structure are successfully fabricated by electrodeposition techniques in order to be applied in fabrication of movable microcomponents in MEMS devices. The Au–Cu alloys are first fabricated by constant current electrodeposition. Surface morphology of the Au–Cu alloy films shows a wide variation from smooth surface to bump-clustered agglomerates as the current density varies from 2 to 9 mA/cm^2. A reduction in the grain size and an increase in the Cu content are observed with an increase in the current density. The film with the finest grain size at 5.3 nm is obtained when current density 6 mA/cm^2 is used. For the microcompression tests, the specimens evaluated are micropillars with dimensions of 10 × 10 × 20 μm^3 fabricated from the electrodeposited Au–Cu alloys. The highest σ_y at 1.15 GPa is achieved for the Au–Cu micropillar having the grain size of 5.3 nm and the Cu concentration of ~30 at%. The yield strength is higher than the values reported in the literatures and suggested to be a synergistic effect of the grain boundary strengthening mechanism with the solid solution strengthening mechanism.

Furthermore, effects of the pulse current parameters on the alloy composition, grain size, surface morphology, and micromechanical property of the Au–Cu alloys are investigated. A wide Cu concentration in the Au–Cu alloys ranging from 10 to 54 at% is obtained. An increase in the Cu concentration is observed by using either or both of a high pulsed current density and a short current off-time. The smallest grain size of ca. 4.4 nm is achieved in films having the Cu concentration ranging from 30 to 40 at%. Grain refinement is achieved with a high J_p, and promoting the displacement reaction could also reduce the grain size. A high J_p results roughening of the surface, and enhancing the displacement reaction leads to a surface smoothening effect. Deformation behavior of the Au–Cu micropillar is affected by the Cu concentration, in which brittle fraction is observed when the copper concentration is higher than 37 at%. An ultrahigh yield strength of 1.50 GPa is obtained in the micropillar having the Cu concentration of 37 at% and the grain size of 4.7 nm. As a result, Au–Cu alloys developed in the present study are suggested to fulfill the requirements to fabricate more sensitive and miniaturized next-generation MEMS devices.

Acknowledgements

This work was supported by JST CREST Grant Number JPMJCR1433 and by the Grant-in-Aid for Scientific Research (S) (JSPS KAKENHI Grant number 26220907).

Conflict of interest

I confirm there are no conflicts of interest.

Author details

Haochun Tang[1], Tso-Fu Mark Chang[1*], Chun-Yi Chen[1], Takashi Nagoshi[2], Daisuke Yamane[1], Toshifumi Konishi[3] and Katsuyuki Machida[1]

1 Institute of Innovative Research, Tokyo Institute of Technology, Yokohama, Japan

2 National Institute of Advanced Industrial Science and Technology (AIST), Ibaraki, Japan

3 NTT Advanced Technology Corporation, Atsugi Kanagawa, Japan

*Address all correspondence to: chang.m.aa@m.titech.ac.jp

References

[1] Seidel H, Riedel H, Kolbeck R, Mück G, Kupke W, Königer M. Capacitive silicon accelerometer with highly symmetrical design. Sensors and Actuators A. 1990;**21**:312-315. DOI: 10.1016/0924-4247(92)80138-S

[2] Ha B, Oh Y, Song C. A capacitive silicon microaccelerometer with force-balancing electrodes. Japanese Journal of Applied Physics. 1998;**37**:7052-7057. DOI: 10.1143/JJAP.37.7052

[3] Okada H, Kobayashi T, Masuda T, Itoh T. Ultra-low power event-driven wireless sensor node using piezoelectric accelerometer for health monitoring. Japanese Journal of Applied Physics. 2009;**48**:070222. DOI: 10.1143/JJAP.48.070222

[4] Mayagoitia RE, Nene AV, Veltink PH. Accelerometer and rate gyroscope measurement of kinematics: An inexpensive alternative to optical motion analysis systems. Journal of Biomechanics. 2002;**35**:537-542. DOI: 10.1016/S0021-9290(01)00231-7

[5] Hong Y-J, Kim I-J, Ahn SC, Kim H-G. Mobile health monitoring system based on activity recognition using accelerometer. Simulation Modelling Practice and Theory. 2010;**35**:446-455. DOI: 10.1016/j.simpat.2009.09.002

[6] Chae J, Kulah H, Najafi K. A monolithic three-axis micro-g micromachined silicon capacitive accelerometer. IEEE Journal of Microelectromechanical Systems. 2005;**14**:235-242. DOI: 10.1109/JMEMS.2004.839347

[7] Abdolvand R, Amini BV, Ayazi F. Sub-micro-gravity in-plane accelerometers with reduced capacitive gaps and extra seismic mass. IEEE Journal of Microelectromechanical Systems. 2007;**16**:1036-1043. DOI: 10.1109/JMEMS.2007.900879

[8] Lemkin M, Boser E. A three-axis micromachined accelerometer with a CMOS position-sense interface and digital offset-trim electronics. IEEE Journal of Solid-State Circuits. 1999;**34**:456-468. DOI: 10.1109/4.753678

[9] Yamane D, Konishi T, Matsushima T, Machida K, Toshiyoshi H, Masu K. Design of sub-1g microelectromechanical systems accelerometers. Applied Physics Letters. 2014;**104**:074102. DOI: 10.1063/1.4865377

[10] Machida K, Konishi T, Yamane D, Toshiyoshi H, Masu K. Integrated CMOS-MEMS technology and its applications. ECS Transactions. 2014;**61**:21-39. DOI: 10.1063/1.4865377

[11] Yamane D, Matsushima T, Konishi T, Toshiyoshi H, Masu K, Machida K. A dual-axis MEMS capacitive inertial sensor with high-density proof mass. Microsystem Technologies. 2015;**22**:459-464. DOI: 10.1007/s00542-015-2539-y

[12] Greer JR, Oliver WC, Nix WD. Size dependence of mechanical properties of gold at the micron scale in the absence of strain gradients. Acta Materialia. 2005;**53**:1821-1830. DOI: 10.1016/j.actamat.2004.12.031

[13] Tsuchiya T, Tabata O, Sakata J, Taga Y. Size dependence of mechanical properties of gold at the micron scale in the absence of strain gradients. Journal of Microelectromechanical Systems. 1998;**7**:106-113. DOI: 10.1109/84.661392

[14] Yamane D, Konishi T, Safu T, Tachibana K, Teranishi M, Chen C-T, et al. Long-term vibration characteristics of MEMS inertial sensors by multi-layer metal technology. In: Proc. 19th International Conference on Solid-State Sensors, Kaohsiung, Taiwan; 18 June-22 June 2017; DOI: 10.1109/TRANSDUCERS.2017.7994510

[15] Rashidi AM, Amadeh A. The effect of current density on the grain size of electrodeposited nanocrystalline nickel coatings. Surface and Coating Technology. 2008;**202**:3772-3776. DOI: 10.1016/j.surfcoat.2008.01.018

[16] Rashidi AM, Amadeh A. The effect of saccharin addition and bath temperature on the grain size of nanocrystalline nickel coatings. Surface and Coating Technology. 2009;**204**:353-358. DOI: 10.1016/j.surfcoat.2009.07.036

[17] Petch NJ. The cleavage strength of polycrystals. Journal of the Iron and Steel Institute. 1953;**174**:25-28

[18] Schuh CA, Nieh TG, Iwasaki H. The effect of solid solution W additions on the mechanical properties of nanocrystalline Ni. Acta Materialia. 2003;**51**:431-443. DOI: 10.1016/S1359-6454(02)00427-5

[19] Li Y, Jiang H, Huang W, Tian H. Effects of peak current density on the mechanical properties of nanocrystalline Ni–Co alloys produced by pulse electrodeposition. Applied Surface Science. 2008;**254**:6865-6869. DOI: 10.1016/j.apsusc.2008.04.087

[20] Chung CK, Chang WT. Effect of pulse frequency and current density on anomalous composition and nanomechanical property of electrodeposited Ni–Co films. Thin Solid Films. 2009;**517**:4800-4804. DOI: 10.1016/j.tsf.2009.03.087

[21] Chang L, Kao PW, Chen C-H. Strengthening mechanisms in electrodeposited Ni–P alloys with nanocrystalline grains. Scripta Materialia. 2007;**56**:713-716. DOI: 10.1016/j.scriptamat.2006.12.036

[22] Yang NYC, Headley TJ, Kelly JJ, Hruby JM. Metallurgy of high strength Ni–Mn microsystems fabricated by electrodeposition. Scripta Materialia. 2004;**51**:761-766. DOI: 10.1016/j.scriptamat.2003.11.001

[23] Maki K, Ito Y, Matsunaga H, Mori H. Solid-solution copper alloys with high strength and high electrical conductivity. Scripta Materialia. 2013;**68**:777-780. DOI: 10.1016/j.scriptamat.2012.12.027

[24] Erdey-Gruz T, Volmer M. Zur theorie der wasserstoff überspannung. Zeitschrift für Physikalische Chemie. 1930;**150**:203

[25] Hamann CH, Vielstich W. Elektrochemie II. Weinheim: Verlag Chemie; 1981. DOI: 10.1002/bbpc.19820860826

[26] Fleischer RL. Substitutional solution hardening. Acta Materialia. 1963;**11**:203-209. DOI: 10.1016/0001-6160(63)90213-X

[27] Labusch R. A statistical theory of solid solution hardening. Physica Status Solidi B: Basic Solid State Physics. 1970;**41**:659-669. DOI: 10.1002/pssb.19700410221

[28] Youssef MS, Koch CC, Fedkiw PS. Influence of additives and pulse electrodeposition parameters on production of nanocrystalline zinc from zinc chloride electrolytes. Journal of the Electrochemical Society. 2004;**151**:C103-C111. DOI: 10.1149/1.1636739

[29] Youssef MS, Koch CC, Fedkiw PS. Influence of pulse plating parameters on the synthesis and preferred orientation of nanocrystalline zinc from zinc sulfate electrolytes. Electrochimica Acta. 2008;**54**:677-683. DOI: 10.1016/j.electacta.2008.07.048

[30] Tury B, Lakatos-Varsanyi M, Roy S. Effect of pulse parameters on the passive layer formation on pulse plated Ni–Co alloys. Applied Surface Science. 2007;**253**:3103. DOI: j.apsusc.2006.06.063

[31] Chang LM, An MZ, Guo HF, Shi SY. Microstructure and properties of Ni–Co/nano-Al_2O_3 composite coatings by pulse reversal current electrodeposition. Applied Surface Science. 2006;**253**:2132-2137. DOI: 10.1016/j.apsusc.2006.06.063

[32] Cahoon JR, Broughton WH, Kutzak AR. The determination of yield strength from hardness measurements. Metallurgical and Materials Transactions. 1971;**2**:1979-1983. DOI: 10.1007/bf02913433

[33] Arzt E. Size effects in materials due to microstructural and dimensional constraints: A comparative review. Acta Materialia. 1998;**46**:5611-5626. DOI: 10.1016/S1359-6454(98)00231-6

[34] Uchic MD, Dimiduk DM, Florando JN, Nix WD. Sample dimensions influence strength and crystal plasticity. Science. 2004;**305**:986-989. DOI: 10.1126/science.1098993

[35] Frick CP, Clark BG, Orso S, Schneider AS, Arzt E. Size effect on strength and strain hardening of small-scale [1 1 1] nickel compression pillars. Materials Science and Engineering A. 2008;**489**:319-329. DOI: 10.1016/j.msea.2007.12.038

[36] Greer JR, Weinberger CR, Cai W. Comparing the strength of fcc and bcc sub-micrometer pillars: Compression experiments and dislocation dynamics simulations. Materials Science and Engineering A. 2008;**493**:21-25. DOI: 10.1016/j.msea.2007.08.093

[37] Uchic MD, Shade PA, Dimiduk DM. Plasticity of micrometer-scale single crystals in compression. Annual Review of Materials Research. 2009;**39**:361-386. DOI: 10.1146/annurev-matsci-082908-145422

[38] Greer JR, De Hosson JTM. Plasticity in small-sized metallic systems: Intrinsic versus extrinsic size effect. Progress in Materials Science. 2011;**56**:654-724. DOI: 10.1016/j.pmatsci.2011.01.005

[39] Dietiker M, Buzzi S, Pigozzi G, Löffler JF, Spolenak R. Deformation behavior of gold nano-pillars prepared by nanoimprinting and focused ion-beam milling. Acta Materialia. 2011;**59**:2180-2192. DOI: 10.1016/j.actamat.2010.12.019

[40] Nagoshi T, Chang T-FM, Tatsuo S, Sone M. Mechanical properties of nickel fabricated by electroplating with supercritical CO_2 emulsion evaluated by micro-compression test using non-tapered micro-sized pillar. Microelectronic Engineering. 2013;**110**:270-273. DOI: 10.1016/j.mee.2013.02.001

[41] Hagen AB, Thaulow C. Low temperature in-situ micro-compression testing of iron pillars. Materials Science and Engineering A. 2016;**678**:355-364. DOI: 10.1016/j.msea.2016.09.110

[42] Imamura H, Nagoshi T, Yoshida A, Chang T-FM, Onaka S, Sone M. Evaluation of anisotropic structure in electrodeposited Ni film using micro-sized cantilever. Microelectronic Engineering. 2012;**100**:25-27. DOI: 10.1016/j.mee.2012.07.118

[43] Clinton JR, Tyler EH, Luo HL. Electrical and magnetic properties of Au–Ni alloys. Journal of Physics F: Metal Physics. 1974;**4**:1162-1169. DOI: 10.1088/0305-4608/4/8/012

[44] Togasaki N, Okinaka Y, Homma T, Osaka T. Preparation and characterization of electroplated amorphous gold–nickel alloy film for electrical contact applications. Electrochimica Acta. 2005;**51**:882-887. DOI: 10.1016/j.electacta.2005.04.057

[45] Raub CJ, Knödler A. The electrodeposition of gold by pulse plating. Gold Bulletin. 1977;**10**:38-44. DOI: 10.1007/bf03215426

[46] Djurfors B, Ivey DG. Pulsed electrodeposition of the eutectic Au/

Sn solder for optoelectronic packaging. Journal of Electronic Materials. 2001;**30**:1249-1254. DOI: 10.1007/s11664-001-0157-1

[47] Jankowski AF, Saw CK, Harper JF, Vallier BF, Ferreira JL, Hayes JP. Nanocrystalline growth and grain-size effects in Au–Cu electrodeposits. Thin Solid Films. 2006;**494**:268-273. DOI: 10.1016/j.tsf.2005.08.149

[48] Brun E, Durut F, Botrel R, Theobald M, Legaie O, Popa I, et al. Influence of the electrochemical parameters on the properties of electroplated Au–Cu Alloys. Journal of the Electrochemical Society. 2011;**158**:D223-D227. DOI: 10.1149/1.3554727

[49] Budevski E, Staikov G, Lorenz WJ. Electrocrystallization: Nucleation and growth phenomena. Electrochimica Acta. 2000;**45**:2559-2574. DOI: 10.1016/S0013-4686(00)00353-4

[50] Gabe DR. The role of hydrogen in metal electrodeposition processes. Journal of Applied Electrochemistry. 1997;**27**:908-915. DOI: 10.1023/a:1018497401365

[51] Bard AJ, Parsons R, Jordan J. Standard Potentials in Aqueous Solution. New York: CRC Press; 1985. ISBN: 9781351414746

[52] Zhang JY, Cui JC, Liu G, Sun J. Deformation crossover in nanocrystalline Zr micropillars: The strongest external size. Scripta Materialia. 2013;**68**:639-642. DOI: 10.1016/j.scriptamat.2012.12.024

[53] Nagoshi T, Mutoh M, Chang T-FM, Sato T, Sone M. Sample size effect of electrodeposited nickel with sub-10 nm grain size. Materials Letters. 2014;**117**:256-259. DOI: 10.1016/j.matlet.2013.12.017

[54] Meyers MA, Mishra A, Benson DJ. Mechanical properties of nanocrystalline materials. Progress in Materials Science. 2006;**51**:427-556. DOI: 10.1016/j.pmatsci.2005.08.003

[55] Marlot A, Kern P, Landolt D. Pulse plating of Ni–Mo alloys from Ni-rich electrolytes. Electrochimica Acta. 2002;**48**:29-36. DOI: 10.1016/S0013-4686(02)00544-3

[56] Roy S, Landolt D. Effect of off-time on the composition of pulse-plated Cu–Ni alloys. Journal of the Electrochemical Society. 1995;**142**:3021-3027. DOI: 10.1149/1.2048679

[57] Bradley PE, Landolt D. A surface coverage model for pulse-plating of binary alloys exhibiting a displacement reaction. Electrochimica Acta. 1997;**42**:993-1003. DOI: 10.1016/S0013-4686(97)83305-1

[58] Ghosh SK, Grover AK, Dey GK, Totlani MK. Nanocrystalline Ni–Cu alloy plating by pulse electrolysis. Surface and Coating Technology. 2000;**126**:48-63. DOI: 10.1016/S0257-8972(00)00520-X

[59] Liu F, Kirchheim R. Nano-scale grain growth inhibited by reducing grain boundary energy through solute segregation. Journal of Crystal Growth. 2004;**264**:385-391. DOI: 10.1016/j.jcrysgro.2003.12.021

[60] Lohmiller J, Woo NC, Spolenak R. Microstructure–property relationship in highly ductile Au–Cu thin films for flexible electronics. Materials Science and Engineering A. 2010;**527**:7731-7740. DOI: 10.1016/j.msea.2010.08.043

[61] Tabor D. The Hardness of Metals. London: Oxford Univ. Press; 1951. ISBN: 9780198507765